Chapter 8
Micro-scale Geometry Measurement

Samanta Piano, Rong Su and Richard Leach

8.1 Introduction

The ability to produce complex, high-precision, miniature components is key to the transition to high-value manufacturing. The advanced manufacturing industries, using precision machining techniques, such as diamond turning, injection moulding, micro-milling and micro-electro-discharge machining, currently have a number of capabilities for measuring small-scale structures with micro-scale tolerances, either with tactile or non-tactile systems [1].

Metrology is essential for the reduction of dimensional tolerances, which allows the production of more efficient machines and the improvement of their longevity by reducing play or wear. An example is smaller and more efficient injection nozzles in combustion machines, which critically depend on improved dimensional measurement capabilities. Further examples are radio frequency or fibre optic connector components, where feature sizes and tolerances require measurement uncertainties at the 0.1 µm level, or small aspherical/freeform lenses in digital cameras or mobile phones [2]. An emerging sector is high-tech medical products, which very often critically depend on small components, for example, in insulin pumps, cardiac pacemakers, in vivo diagnostic sensors or medical endoscopic imaging systems.

In this chapter, contact and non-contact techniques that can be used to measure 3D features on the micro-metre scale are reviewed.

S. Piano (✉) · R. Su · R. Leach
Manufacturing Metrology Team, Faculty of Engineering, University of Nottingham,
University Park, Nottingham NG7 2RD, UK
e-mail: Samanta.Piano@nottingham.ac.uk

R. Su
e-mail: Rong.Su@nottingham.ac.uk

R. Leach
e-mail: Richard.Leach@nottingham.ac.uk

© Springer International Publishing Switzerland 2017

I. Fassi and D. Shipley (eds.), *Micro-Manufacturing Technologies and Their Applications*, Springer Tracts in Mechanical Engineering,
DOI 10.1007/978-3-319-39651-4_8

8.2 Contact Techniques

Stylus instruments and coordinate measuring machines are widely used in modern manufacturing processes as accurate and precise dimensional measuring tools. This section describes the main characteristics of contact techniques, focusing on their capability to measure micro-scale manufactured parts.

8.2.1 Stylus Instruments

A stylus instrument consists of a sharp tip placed in contact with the surface being measured. By scanning the tip across the surface and monitoring its response to surface heights, it is possible to measure surface topography. A schema of a stylus instrument is shown in Fig. 8.1.

As the stylus tip is scanned across the surface, its vertical displacement is recorded in order to produce a height map and converted into an electrical signal using an electro-mechanical transducer [3–6]. The tip plays a critical role in the performance of a stylus instrument as it is in physical contact with the surface. The stylus tip is usually made of diamond but other materials, such as aluminium oxide, are often employed depending of the material of the surface being measured. Other parameters that should be taken into account are the shape and size of the stylus tip, which directly affect the spatial frequency response of the instrument. Depending on the application, the stylus tip can have different geometries; the most frequently used has a conical shape with a rounded contacting edge and radius of curvature ranging from 2 to 10 µm, and a 90° slope angle [7].

One effect that should be taken into account is the systematic error associated with the shape of the stylus tip that will distort the measured topography [8, 9]. This issue has been intensively studied, and mathematical models have been proposed to include

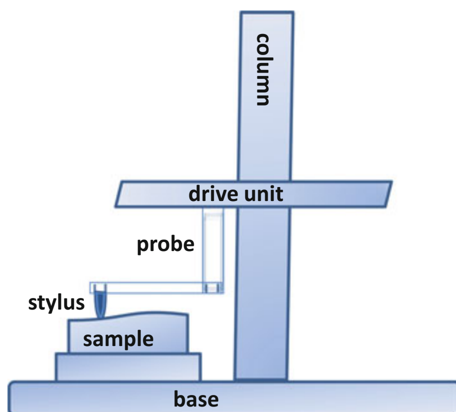

Fig. 8.1 Schema of a stylus instrument

the distortion effect and improve the accuracy of measurements [10–12]. The ability of a contact stylus to detect samples with steep surfaces has also been a subject of investigation; for this a new slope-adapted sample-tilting method has recently been proposed, showing a significant reduction of the measurement error [13].

Although stylus instruments are widely used for surface profile measurement, if used with a large radius spherical tip, such an instrument can also be used to measure surface form. However, use of a stylus instrument for 3D measurements in a production or in-line process is limited due to the operating time, which can be up to several hours for a high-density grid of points.

8.2.2 *Micro Coordinate Measuring Machines*

8.2.2.1 Introduction to Coordinate Measuring Machines

A coordinate measuring machine (CMM) measures the physical dimensions of an object [14]. As shown in Fig. 8.2, a CMM generally consists of three orthogonal linear axes for accurate movement of a probe in a Cartesian coordinate system.

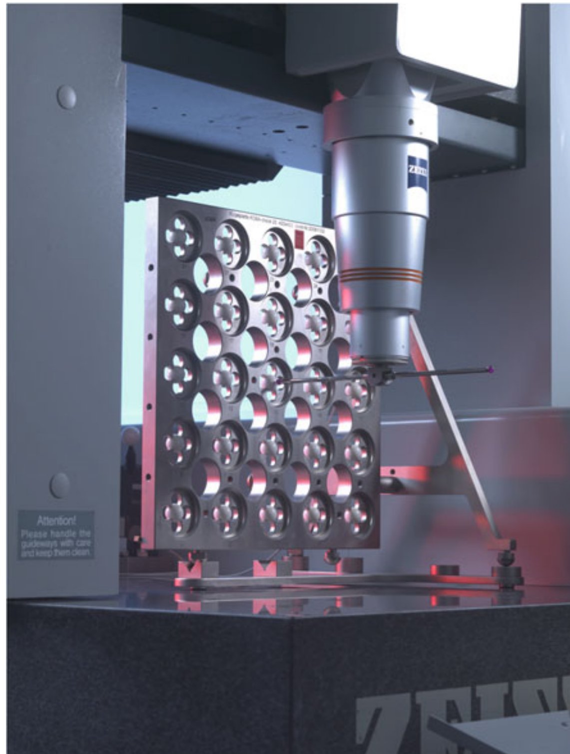

Fig. 8.2 Moving bridge type CMM with spherical styli. Image courtesy of Mr. David Flack at the National Physical Laboratory

The probe on a CMM usually has a spherical stylus tip that is used to contact the object being measured. The coordinates of the stylus tip are registered when in contact with the surface of the object being measured. After compensation for the stylus radius, the coordinates of the surface can be determined.

There are many different geometrical configurations of CMM that use different moving bridges and rotary tables [4]. Some configurations may have additional rotational axes [15]. A modern CMM is usually operated using computer numerical control (CNC) software. This allows for automated 3D measurement if the CMM is programmed with input from a computer-aided design (CAD) model of the part being measured.

8.2.2.2 Capability of Commercial Micro-CMMs

The increased demand on the manufacture of micro-scale products requires CMMs to be able to measure micro-scale parts accurately. So-called "micro-CMMs" have been developed to meet this demand. Generally, a micro-CMM can be designed by miniaturisation of the traditional CMM or using a probe that employs optical technology. State-of-the-art micro-CMMs typically have working ranges of tens of millimetres with hundreds of nano-metre volumetric accuracy, and can be used to measure features with milli-scale to micro-scale dimensions. Typical examples of commercial systems are the Zeiss F25 micro-CMM [16] the IBS Isara 400 Ultra precision CMM [17] and the SIOS Nano-measuring Machine (NMM) [18]. The Zeiss F25 CMM has a measurement volume of 100 mm × 100 mm × 100 mm, and a maximum permissible error (MPE) statement of 0.25 + L/666 μm, where L is the measurement length in millimetres. The Isara 400 minimises the Abbe error [19] by aligning three linear interferometers to the centre of the stylus tip. The measurement volume is 400 mm × 400 mm × 100 mm, and the stated 3D measurement uncertainty is 109 nm (at k = 2). The NMM is a laser interferometer-based micro-CMM developed by the Ilmenau University of Technology. The measurement range is 25 mm × 25 mm × 5 mm with a sub nano-metre resolution of motion. In addition, several other micro-CMMs exist and several reviews of existing micro-CMMs can be found elsewhere [4, 20, 21].

8.2.2.3 Micro-probing Systems

One of the most important components of a micro-CMM is the probing system. The probing system is defined in ISO 10360 part 1 [22] for conventional tactile CMMs and Fig. 8.3 shows the main components. In general, probe technologies for micro-CMMs include mechanical probes, silicon-based probes, opto-mechanical probes and vibrating probes. An in-depth review of micro-CMM probes can be found elsewhere [23].

Mechanical micro-CMM probes are based on the same concepts as classical CMM probes, but they are highly-refined and optimised for sensitive detection and low-force probing. As styli with 100 µm or smaller diameters become available, the measurement is highly sensitive to the probing force. Reducing the probing force may reduce the possible damage caused by plastic deformation and increase the accuracy of the measurement significantly.

Examples of mechanical micro-CMM probes include the probe developed at METAS, which relies on precision flexure hinges and inductive sensors [24], the IBS Triskelion (three-legged) design and highly sensitive capacitors [17], and the 3D mechanical probe design that uses DVD pickup heads as the sensing element [25]. The IBS Triskelion and METAS probes are shown in Fig. 8.4.

The advantage of silicon-based probes is the reduced probing force by using silicon flexures, membranes or meshes to suspend the stylus [26]. Production techniques from the integrated circuit industry are used to design and manufacture silicon-based micro-probes. Highly complex designs are enabled by etching and deposition techniques.

The displacement of the stylus can be detected by using optical detection based on deflection of a laser beam, interferometric measurements, a capacitive sensor, or a piezo-resistive strain sensor on silicon flexure or membrane. For example, Physikalisch-Technische Bundesanstalt (PTB) developed the “Boss-probe” where piezo-resistive strain sensors are etched onto silicon membrane (as shown in Fig. 8.5). The deformation that results from probe contact with the surface being measured is detected [27].

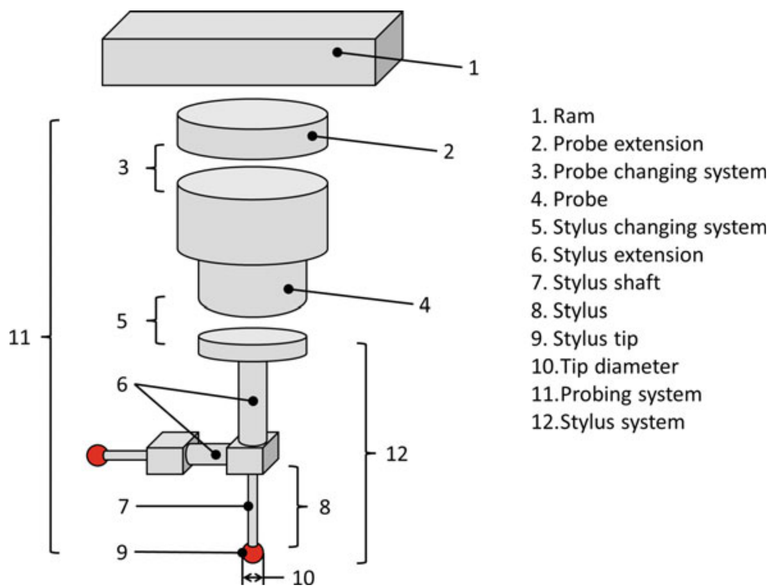

Fig. 8.3 Typical tactile probe and stylus system

Fig. 8.4 The IBS Triskelion [17] and METAS micro-CMM probes [24]

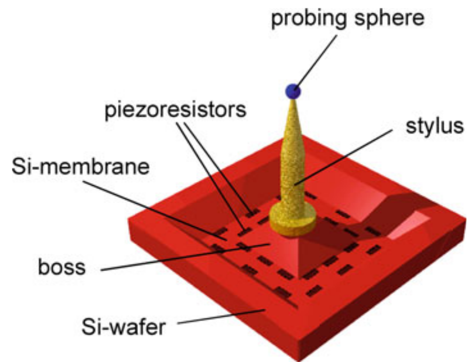

Fig. 8.5 Schema of the Boss-probe developed at PTB [27]

Details of other silicon-based micro-probes can be found elsewhere [28, 29]. A problem with silicon-based micro-CMM probes is anisotropy of probe stiffness. Opto-mechanical probes are designed to address this problem and the need for low force probing. Opto-mechanical probes rely on optical measurement of the stylus tip that is in contact with the surface being measured, so that flexure elements are not needed.

A probing system designed by PTB [27] uses an optical fibre with a spherical tip as the stylus. As shown in Fig. 8.6, two microscope objectives are used to measure the movement of the probe tip in the x, y and z axes. The measuring force of this fibre probe is on the order of 10 µN. However, the probe tip is likely to stick to the surface being measured, and probing forces are not isotropic. Another example of an optical fibre probe has been developed at the National Institute for Standards and Technology [30].

Vibrating micro-CMM probes have been designed and developed to address the problem of surface interaction forces, which become significant when a stylus tip diameter is of the order of 100 µm and lower. The influences of surface interaction forces can be reduced by using a vibrating probe tip, and the problem of sticking is

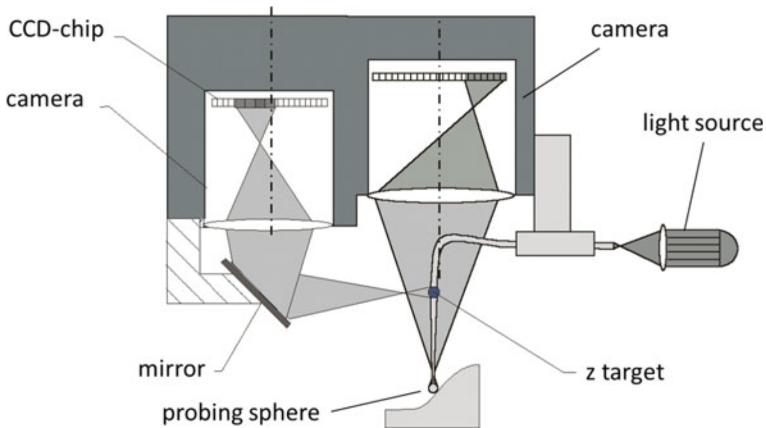

Fig. 8.6 Schema of the 3D PTB fibre probe [27]

minimised. With vibrating probes, the surface is measured by analysing the detected vibration characteristics.

An example of a commercial vibrating micro-CMM probe is the UMAP system from Mitutoyo [23]. The UMAP probe vibrates the stylus vertically at several kilohertz. The estimated repeatability of the system is about 100 nm, which is often not suitable for high-accuracy measurement. Other vibrating probes with nano-metre repeatability and/or nano-newton contact force exist [31, 32]. There are various methods to vibrate the probe tip, for example, oscillation at a frequency of several tens of kilohertz by a quartz oscillator, or by laser trapping an 8–10 μm diameter silica sphere and vibrating the probe in the z axis at frequencies up to 50 MHz [31].

These vibrating probes can only oscillate in one dimension. A 3D vibrating micro-CMM probe has been developed at the National Physical Laboratory (NPL) [33], see Fig. 8.7. The NPL probe consists of a triskelion flexure and a micro-stylus, and vibrates by using six piezoelectric (PZT) actuators.

8.2.2.4 Sources of Error on CMMs

A typical CMM has twenty-one sources of geometric error [4]. Each axis has a linear error, three rotation errors and two straightness errors (six per axis gives eighteen). The final three errors are the orthogonality errors between any two pairs of axes. The CMM geometric errors are measured in one of the four following manners:

- using instruments such as straight edges, autocollimators and levels;
- using a laser interferometer system and associated optics;
- using a calibrated-hole plate [34]; and
- using a tracking laser interferometer [35].

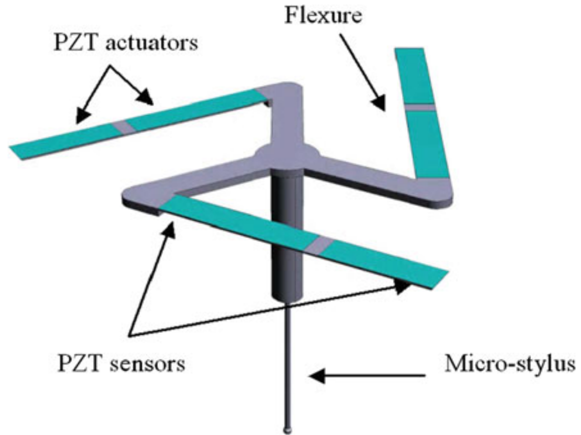

Fig. 8.7 NPL vibrating micro-probe [33]

With modern computers, CMMs can be error-mapped (volumetric error compensation) with corrections to geometric errors made in software [36, 37]. Temperature dependent measurement error can be compensated using a parametric approach [38]. The measurement uncertainty of a CMM can be assessed by using a simulation method [39]; CMM software also needs to be tested based on ISO 10360 part 6 [40].

8.3 Non-contact Techniques

There are different types of commercial non-contact techniques. This section focuses on optical instruments that are suitable to measure 3D micro-systems: focus variation microscopy, coherence scanning interferometry, confocal microscopy, laser triangulation and micro-fringe projection. In contrast to traditional contact techniques, optical instruments are able to perform 3D measurements without touching the surface, they can be much faster when imaging over an area and can determine colour information.

8.3.1 Focus Variation Microscopy

Focus variation (FV) microscopy provides information about the topography and colour of a measured surface [41, 42]. FV is able to perform high-resolution form and texture measurements [43]. A schema of a FV microscope is given in Fig. 8.8.

In a typical FV microscope, the light generated by a broadband source, is focused onto the sample through a system of objective lenses and a beam-splitting mirror. The light is scattered from the sample into different directions depending on

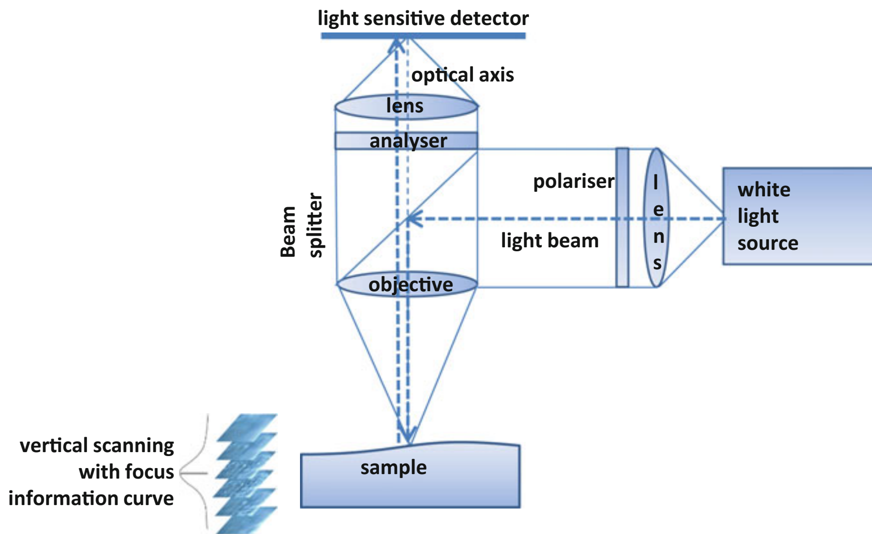

Fig. 8.8 Schema of a focus variation microscope, adapted from [42]

the topography. The scattered light reaching the objective lenses is then transmitted through the beam-splitting mirror and received by a light sensitive detector. In order to have a 3D complete map of the surface of the sample, the objective lenses are moved vertically along the optical axis. Due to the surface topography, only a single plane will be in focus, resulting in a changing of contrast on the light sensitive detector. Algorithms are used to analyse the variation of the focus in the vertical axis in order to convert the acquired data into 3D information and a colour image of the sample [44, 45]. The vertical scan range, depending on the working distance of the objective, can vary from 3.2 to 22 mm, with a resolution as high as 10 nm. The xy range typically varies from around 0.1 mm × 0.1 mm to 5 mm × 5 mm for a single measurement (depending on the objective), but can be increased up to 100 mm × 100 mm by using stitching algorithms and a motion stage. The FV technique can be used to measure samples with high slope angles, exceeding 80° [46].

Relying on the contrast and sharpness in the images taken from the measurements to determine the point of focus, the FV technique is limited to surfaces with a certain degree of roughness (or needs another contrast-generating mechanism).

8.3.2 Coherence Scanning Interferometry

Coherence scanning interferometry (CSI) refers to low coherence interferometry techniques, also known as scanning white light interferometry, coherence cor

synchrotron, XCT relation interferometry and vertical scanning interferometry [47–49]. Many other terms are used to refer to CSI, but they all refer to the same fundamental principle that uses the coherence property of light to measure surface topography and object geometry.

As shown in Fig. 8.9, a typical CSI system contains a broadband source for generation of low temporal coherence illumination, a CCD camera for capturing the image, and an interferometer with a high-precision motion system (often PZT) for axial scanning of the reference mirror [48]. Usually a Mirau interferometer configuration is used when employing a high-magnification objective lens and a Michelson interferometer is used with a low magnification lens.

The operating principle of CSI is based on low coherence interferometry; where the interference signal is generated when the reference and sample beam have equal optical path length. The peak position of the interference signal corresponds to the position of the sample surface. By scanning the reference mirror, the sample surface is scanned axially and a height map is established. The details of the operating principle can be found elsewhere [48]. Usually the interference signal received by a pixel of the camera is similar to that shown in Fig. 8.9b. The signal is a sinusoidal carrier that is modulated by a slowly varying modulation envelope. The surface location can be extracted as the peak position of the envelope of the interference

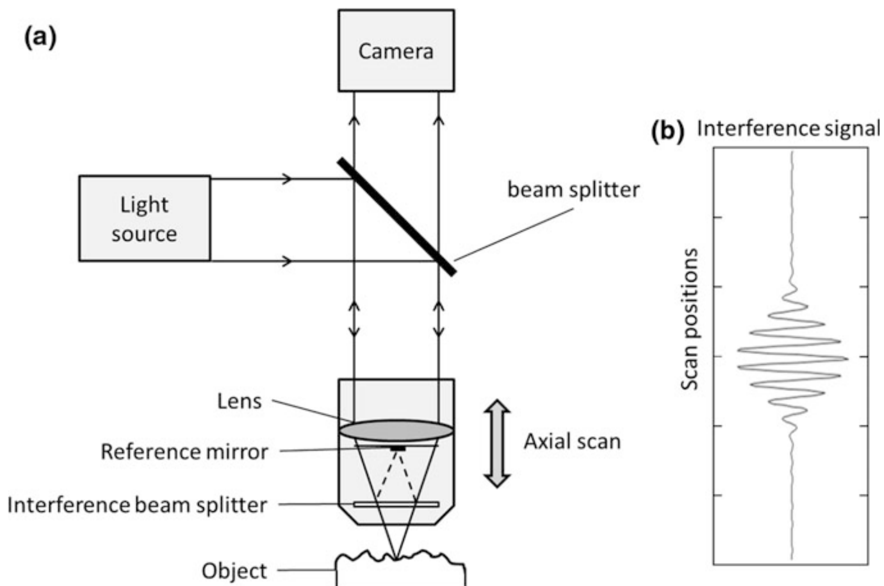

Fig. 8.9 Schema of a CSI system with Mirau objective (**a**) and simulation of the CSI signal recorded by a pixel (**b**)

signal or by the centroiding method that is more robust against noise in some cases [47]. Most modern CSI instruments combine envelope detection with interference phase information to improve the precision [50]. After signal processing, the extracted height at each pixel forms the measured height map of the surface. Typically, the field of view (FOV) is from around 0.1 mm × 0.1 mm to 4 mm × 4 mm (depending on the objective), and the scanning depth is around a few hundred micro-metres. Larger FOVs can be achieved at the cost of sacrificing lateral resolution [51]. Stitching techniques may increase the measurement range in the lateral and axial directions [52], but the accuracy will degrade and be dependent on the accuracy of the motion system and data processing.

Sub-nano-metre axial resolution and repeatability can be achieved in modern CSI systems, but the absolute accuracy is difficult to determine [53]. The accuracy is influenced by the interaction between the light and different materials with different optical properties. For example, for a flat surface containing multiple materials, a pseudo height effect can be observed which is caused by the phase change on reflection [48].

CSI techniques can also operate without mechanical axial scanning, which is carried out by means of spectroscopic analysis or wavelength scanning [54, 55]. Wavelength scanning interferometry may increase the measurement speed and be used for in-line applications requiring high immunity to external vibration [56].

A recent development is model-based CSI. This development allows for measurement of semi-transparent thin film thickness and features with lateral critical dimensions on nano-metre scales, which is smaller than the diffraction limit [57]. Model-based CSI has found application in the semiconductor and flat panel display industries [58].

8.3.3 Confocal Microscopy

The principle of confocal microscopy (CM) was originally developed by Minsky in the mid-1950s [59, 60], and the first commercial instrument appeared in 1987. The development of CM has been possible thanks to progress in optics and electronics, and today it is a 3D optical imaging technique used in many applications, from semiconductor materials to life science systems [61–63]. Depending on the application, different CM configurations have been proposed and realised, varying in the way to illuminate the sample and/or to detect the returning beam. It is possible to distinguish three categories of CM: laser scanning, disc scanning and array scanning [64]. The principle of CM is illustrated in Fig. 8.10.

In a typical laser scanning CM, the light emitted by a laser illuminates the sample after passing through a pinhole aperture, a beam-splitter and an objective lens. The light reflected back from the sample is incident on the detector after passing through a second pinhole, which minimises the effect of the out-of-focus light. In this way, only the in-focus light is recorded and contributes to the

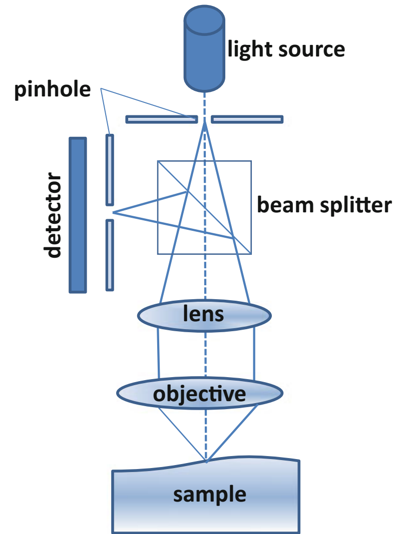

Fig. 8.10 Confocal microscopy set-up with the sample in focus

reconstruction of the sample topography. The image created by CM is a planar section of the sample and the 3D topography of the sample is obtained by scanning the sample along the optical axis and reconstructing the 2D images.

The resolution of a CM depends on the diffraction limit and can be further enhanced by reducing the size of the pinholes, via the so-called "pinhole effect" [64]. For larger pinhole size, the confocality degrades and the signal is broadened, on the other hand the pinhole size cannot be reduced arbitrarily because this also reduces the incident light intensity and consequently the signal-to-noise ratio [65]. In particular, for pinhole sizes larger than 0.25 AU (AU = Airy unit, defined as the diameter of a diffraction-limited spot on the plane of the objective), the instrument is in the regime of geometric-optical confocality and the lateral resolution is given by the radius of the Airy disk, defined as the distance from the centre of the bright spot to the centre of the first dark ring [64, 66, 67]

$$R_{Airy} = 0.61\frac{\lambda}{A_N}, \tag{8.1}$$

where λ is the wavelength of the light and AN is the numerical aperture. For pinhole sizes smaller than 0.25 AU, the instrument is in the wave-optical confocality regime, where the effects of diffraction have to be taken into account, which results in an enhanced lateral resolution given by [64]

$$R_{Airy} = 0.37\frac{\lambda}{A_N}, \tag{8.2}$$

where λ is the wavelength of the incident light and AN is the numerical aperture.

The lateral resolution thus varies typically between 0.25 μm (blue light source) and 1.5 μm (red light source) [4]. The axial resolution, instead, is defined by the full width at half maximum of the point spread function of the Airy disk, and is given by [64]

$$R_{axial} = \sqrt{\left(\frac{0.88\lambda}{1 - \sqrt{1 - A_N^2}}\right)^2 + \left(\frac{\sqrt{2}d_{hole}}{A_N}\right)^2}, \tag{8.3}$$

in the geometric-optical confocality regime (where d_{hole} is the size of the detection pinhole), and

$$R_{axial} = \frac{0.64\lambda}{1 - \sqrt{1 - A_N^2}}, \tag{8.4}$$

in the wave-optical confocality regime.

The measurement speed of CM depends on the time it takes to scan in the xy direction; a laser scanning microscope needs to scan point by point and usually can generate 5–10 images per second (512 × 512 pixels per image) [64]. Disc scanning and micro-display scanning CMs are often much faster than a scanning system using galvo-mirrors [4].

Unlike the other optical techniques in this chapter, CM has a high numerical aperture, which leads to a high lateral resolution. Moreover, due to the pinhole effect, the resolution can be increased over the limits defined by the Abbe criterion [4]. The CM is also able to measure high local slope angles, that for rough surfaces can be close to 90° [64]. Furthermore, CM instruments are able to measure surfaces containing dissimilar materials without the need for any correction of the measurements.

8.3.4 Laser Triangulation

In laser triangulation (LT) a light pattern, generated from a laser, is projected on to an object and the reflection is captured by a digital camera [68]. A typical configuration of a LT system is shown in Fig. 8.11.

With reference to Fig. 8.11, if (x, y, z) is a 3D point on the object illuminated by the laser light, and f is the focal length of the lens, its projection (x′, y′) on the image plane will be x′ = xf/z, y′ = yf/z. By knowing the baseline distance d and the angle θ between the laser and the lens, which obey the condition

$$d = \frac{z}{\tan\theta}, \tag{8.5}$$

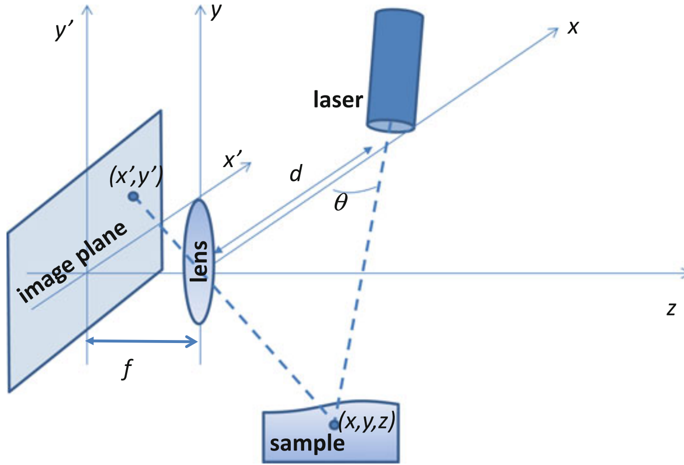

Fig. 8.11 Principle of laser triangulation

it is possible to define the real coordinates (x, y, z) in terms of the focal length f and the angle θ,

$$x = \frac{dx'}{f\cot\theta - x'}, y = \frac{dy'}{f\cot\theta - x'}, x = \frac{df}{f\cot\theta - x'}. \tag{8.6}$$

To have a complete map of the object, images are captured for different values of θ and for each image the values of x′ and y′ are determined on the CCD camera. The real coordinates are calculated using Eq. (8.6).

Due to its simplicity, the LT method is used in many sensors with applications ranging from measuring surfaces with large structures [4], to fuel cells [69] and plant phenotypes [70]. Different configurations of LT have been proposed in order to improve the resolution and the accuracy of the measurements. For example, some authors proposed to use two colour lasers to minimise the occlusion problem in the direction of movement of the camera [71]. The main advantages of LT are: the measuring speed, i.e. data rates up to 10,000 measurements per second, and the accuracy, as some sensors report a resolution of 2000:1–20,000:1 [72], in other words for a few millimetres range is it possible to achieve a sub micro-metre vertical resolution [4].

Despite its advantages, the LT technique has some inherent limitations that should be taken into account in order to obtain reliable information from the measured data. In principle, the laser spot should be infinitely small, but in practice it has a finite size. Also, due to the focus of the laser beam, its diameter can vary along the vertical scan. Moreover, as a consequence of some imperfections of the laser system, blur [73] and shadow [74] effects can appear in the image. Further sources of error are associated with the tilt angle of the surface, edge effects and

linearity errors [27]. A complete knowledge and understanding of the error sources should help to overcome some of the limitations of these sensors, making them suitable for many applications in micro-manufacturing.

8.3.5 Micro-fringe Projection

In a fringe projection (FP) instrument, a structured pattern, for example, a sinusoidal fringe pattern, is generated by a computer and projected onto the object to be measured [75]. The fringes, deformed by the object surface topography, are recorded by a camera and sent to a computer. The fringe data is analysed to obtain 3D shape information about the object. In Fig. 8.12, a typical schema of a FP instrument is shown.

The FP technique is typically used to measure objects from the metre to the millimetre scale and its first application to the micro-scale was proposed by Leonhardt et al. [76]. Even though the use of FP on the micro-scale is increasing, there have been only a small number of applications reported to date (see for example [77–82]). Micro-FP is generally based on a modification to a stereo microscope [81], or by employing a long working distance objective lens [83]. Because different types of lens can be used, the latter technique is more flexible and can be used in many different applications [82].

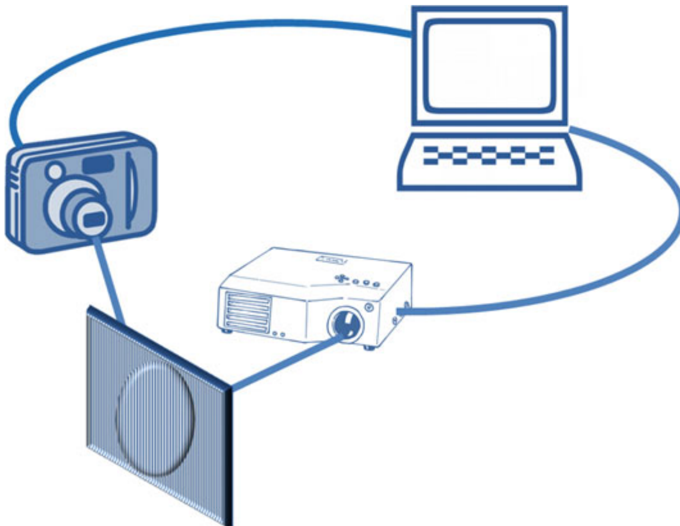

Fig. 8.12 Schema of a fringe projection instrument

The FP techniques differ in the way they generate the fringe pattern and in the methods used to analyse the fringe pattern [75]. Another important aspect of the FP technique is the calibration of the system in order to allow a measurement of the 3D height distribution, and different approaches have been proposed [75, 82].

Some authors have shown that, by using a FP technique, it is possible to measure a micro-V-groove with a size of 150 μm × 250 μm and an angle larger than 45° with an error below 1% of the full-scale measurement range [78]. Others report that with a phase-shifting detection scheme it is possible to achieve accuracy better than one part in ten thousand of the FOV [78]. The resolution of the optics and the camera determine the lateral and vertical resolution in FP. The vertical resolution is also determined by the frequency of the projection pattern. A typical vertical resolution for FP systems is of the order of 1 μm [82].

8.4 Tomographic Methods

The word tomography is derived from the Ancient Greek word "tomos"; meaning to slice and section. Usually tomographic imaging is referred to a 3D imaging method that is able to obtain dimensional and material information of the internal and external features of an object. Two tomographic methods suitable for micro-manufactured parts are introduced in this section, namely optical coherence tomography and X-ray computed tomography.

8.4.1 Optical Coherence Tomography

Optical coherence tomography (OCT) has been growing in popularity since 1991 [84]. OCT uses non-invasive detection and produces depth-resolved high-resolution 2D or 3D images of the back-scattering from internal micro-structures in an object. In general, OCT is based on the principle of low-coherence reflectometry and measures the "echoes" of backscattered light. As a tomographic imaging modality, a series of 1D depth z-scans, similar to ultrasound A-scans, are performed pointwise along a line in the lateral x-direction. By combining these scans for a given y-position, a 2D cross-sectional image (B-scan) is obtained in the xz plane. By further combining these cross-sectional images recorded at adjacent y-positions, a full 3D tomographic image can be obtained. OCT is a complementary method to other high-resolution 3D imaging techniques, such as ultrasound imaging, X-ray computed tomography (XCT) and magnetic resonance imaging (MRI).

Biomedical and clinical applications are the conventional driving force of OCT development, for example, real-time in vivo visualisation of tissue microstructures in eyes, arteries and nervous tissues [84]. However, new applications have spread broadly outside the biomedical field into materials investigation. Detailed overviews of OCT-based methods and applications in the fields of dimensional

metrology, materials research, non-destructive testing, art diagnostics, botany, micro-fluidics, data storage and security applications can be found elsewhere [85]. Specifically, OCT is suitable for detection of sub-surface and embedded features inside dielectric materials, such as glasses, plastics, polymers, ceramics and additive manufacturing materials [86]. The signal acquisition rate of OCT is high and has grown from two A-scans per second in the original version in 1991 to today's megahertz technology [87]. This advantage of high speed imaging shows potential for roll-to-roll manufacturing of ceramic micro-devices, printable electronics [88] and polymer solar cells [89]. The typical resolution of OCT is of the order of 10 µm for both the axial and lateral directions.

OCT is usually divided into two groups: time-domain OCT (TD-OCT) and Fourier-domain OCT (FD-OCT). The principle of TD-OCT is very similar to CSI (see Sect. 1.3.2) but operates in the infra-red part of the spectrum. In the past decade, FD-OCT has attracted more attention and been developed rapidly. The most important advantage over traditional TD-OCT is that FD-OCT offers the possibility of much faster imaging speeds and higher detection sensitivities. Mechanical scanning of a reference mirror is no longer needed in FD-OCT. An A-scan is obtained by a Fourier transform of the spectrally-resolved interference fringes detected by using a spectrometer, for example, a line array camera. Such a system is called spectral-domain OCT (SD-OCT). Another option is swept-source OCT (SS-OCT), which uses a swept laser source (wavelength-tuning) with a single photodetector to record the spectrally-resolved interference fringes sequentially, while tuning the wavelength. More details of the principle of OCT can be found elsewhere [84]. A schema of SS-OCT is shown in Fig. 8.13 and a typical volumetric OCT image is shown in Fig. 8.14.

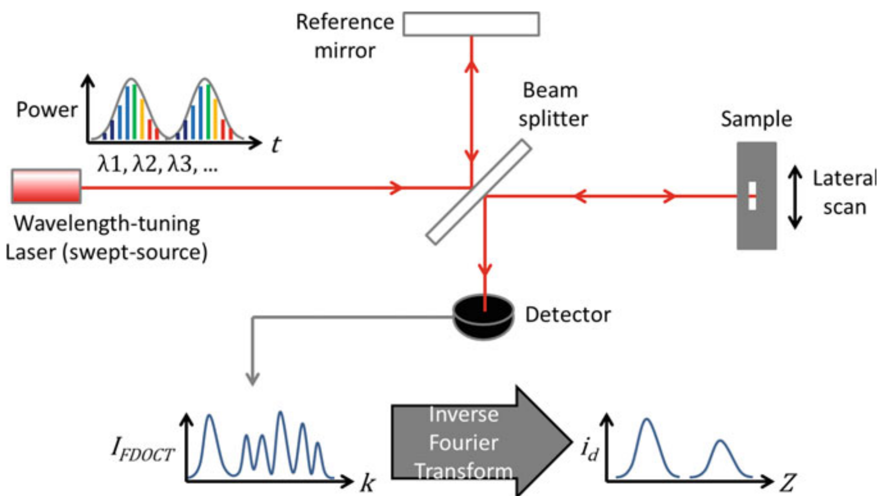

Fig. 8.13 Schematic setup of a swept-source OCT

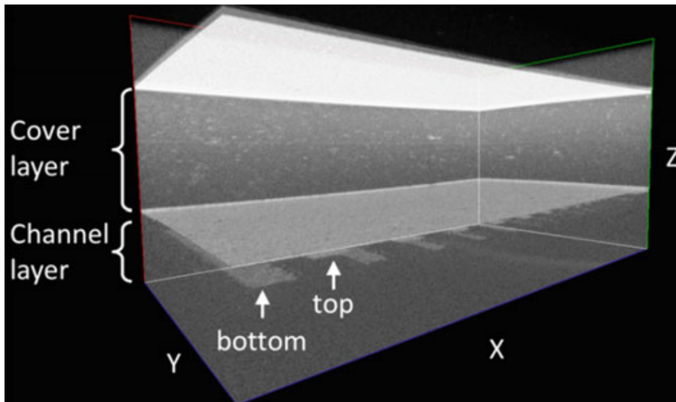

Fig. 8.14 Volumetric OCT image of a two-layer ceramic stack (image rendered for visualisation). A micro-machined channel layer is embedded beneath a zirconia layer. The z axis represents optical distance [90]

Various functional OCTs have been developed, including Doppler OCT [91], which measures the displacement of an object or flow, polarisation-sensitive OCT [92], which measures the birefringence properties of materials, ultrahigh-resolution full-field OCT, which produces tomographic images in the en-face orientation with micro-metre resolution for both axial and lateral directions [93], endoscopic OCT, which performs radial scanning [94], and a second harmonic generation (SHG) microscope combined with OCT for the investigation of subsurface regions of corrosion sites formed on metals below organic coatings [95].

The major problem regarding dimensional metrology and defect detection using OCT is the limited penetration of light due to high scatter. The central operating wavelengths of modern commercial OCT setups are usually around 800, 1300 nm or 1550 nm, which are optimised for the optical transparency window in biomedical tissues and take advantage of well-established optical communication technologies. However, for industrial applications, different wavelengths may be more suitable, for example the mid-infrared region for ceramic materials [96].

The uncertainty of dimensional measurement by OCT is difficult to determine. Speckle degrades image quality significantly [97]. The group velocity dispersion may degrade the axial resolution and the detection sensitivity [98]. Wavefront distortion from the scanning optics, image ambiguity due to inhomogeneity of the refractive index of the material being measured and multiple reflection effects have been observed [90]. Image analysis is also essential for ensuring the accuracy of surface segmentation [99].

8.4.2 X-ray Computed Tomography

X-ray computed tomography (XCT) is a powerful 3D imaging tool that has been used for clinical and industrial applications for decades. Industrial XCT has attracted much attention in recent years as it is promising for non-destructive dimensional metrology of micro-manufacturing parts with complex internal cavities and lattice structures, for quality inspection of complex assembled products and for checking interfaces of multi-material components [100, 101]. XCT is widely used for various applications due to the good penetration of X-rays in many engineering materials.

An XCT system usually contains an X-ray tube, a manipulation system, a detector and a computer [102]. Electrons are accelerated in the X-ray tube and hit an anode target (usually tungsten) to generate X-rays [103]. The highest energy of the X-rays is determined by the peak tube voltage, which usually ranges from 20 to 450 keV in commercial XCT systems [101]. Synchrotron sources that generate monochromatic X-rays can also be used for tomographic imaging [104], but at a much higher cost.

XCT detectors usually consist of a 1D or 2D array of pixels, corresponding to line detectors and flat panel detectors, respectively. A typical flat panel detector contains 2048 × 2048 pixels for an area of 400 mm × 400 mm. Most detectors use a scintillator to convert X-rays to visible light that can be captured by a camera [105]. Alternatively, ionization detectors that respond to energy deposition per unit mass can be used [105].

The manipulation system is used for translating and rotating the object being measured. A few thousand 2D X-ray radiographs, taken from different angles of an object, are recorded for further 3D reconstruction of the tomographic image using the Fourier slice theorem. The reconstruction is usually carried out by filtered back-projection, which is based on the linear integral transformation model developed by Radon [102, 106]. Different amounts of X-rays are absorbed when passing through different materials corresponding to the linear attenuation coefficients of the materials at a certain X-ray energy level. The linear attenuation coefficient is the desired value after reconstruction and relates to the material mass density.

Among the family of XCT systems, poly-energetic cone-beam XCT (CBCT) is used widely in both medical and industrial applications (as shown in Fig. 8.15). The magnification of the object relies on a simple principle of geometrical optics, i.e. a point source is assumed and the magnified projection of the object is dependent on the distance between the source and the object. A survey of different reconstruction methods for CBCT can be found elsewhere [106]. The scanning time of CBCT usually ranges from 30 min to a few hours. It is very difficult to achieve traceability in XCT due to the high number of influence factors and the stability of many set-ups. The most common systematic errors include geometrical errors [107], beam drift due to thermal expansion of the X-ray tube [108], beam hardening effects caused by errors in the estimation of the attenuation coefficient of the material

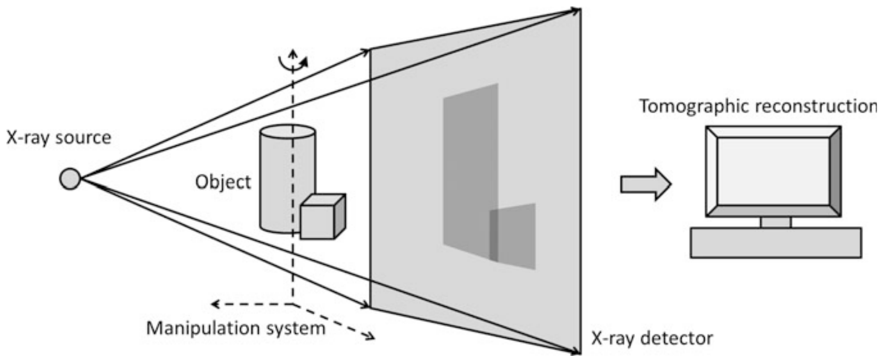

Fig. 8.15 Schema of a CBCT system

[109], partial volume artefacts caused by the limited field of view of the XCT system [110], and errors due to effects of scattering [111] and image lag [112]. Recently several studies and international comparisons have been conducted on uncertainty evaluation of XCT for dimensional measurements [113–115].

Industrial XCT is a fast growing technique. The scanning time is reduced significantly due to advances in XCT components and computing power. Several methods are available for extending the scanning field of view [116]. Multi-energy XCT may differentiate materials by using different X-ray spectra or energy-resolved detectors [117]. Phase-sensitive XCT can be used to enhance image contrast and edges of structures [118].

For micro-manufacturing, the spatial resolution of XCT is important. The resolution is influenced by many factors, for example focal spot size of the X-ray source, quality and pixel size of the detector, magnification of the image, and reconstruction algorithms [119]. Micro or nano-metre-scale imaging resolutions are achieved in state-of-art XCT systems [120]. By applying Kirkpatrick–Baez optics a synchrotron, XCT can reach 40 nm resolution [104].

References

1. Tosello G, Hansen HN, Marinello F, Gasparin S (2010) Replication and dimensional quality control of industrial nanoscale surfaces using calibrated AFM measurements and SEM image processing. Ann CIRP 59:563–568
2. Fang FZ, Zhang XD, Weckenmann A, Zhang GX, Evans C (2013) Manufacturing and measurement of freeform optics. Ann CIRP 62:823–846
3. ISO 25178 part 601 (2010) Geometrical product specifications (GPS)—surface texture: Areal–Part 601: Nominal characteristics of contact (stylus) instruments. International Organization for Standardization
4. Leach RK (ed) (2014) Fundamental principles of engineering nanometrology, 2nd edn. Elsevier, Amsterdam

5. Whitehouse DJ (2010) Handbook of surface and nanometrology, 2nd edn. CRC Press, Florida
6. Thomas TR (1999) Rough surfaces, 2nd edn. Imperial College Press, London
7. Leach RK (2001) The measurement of surface texture using stylus instruments. NPL Good Practice Guide. National Physical Laboratory, UK
8. Radhakrishnan V (1970) Effect of stylus radius on the roughness value measured with tracing stylus instruments. Wear 16:325
9. McCool JI (1984) Assessing the effect of stylus tip radius and flight on surface topography measurements. ASME J Tribol 106:202–209
10. Mendeleyev V (1997) Dependence of measuring errors of rms roughness on stylus tip size for mechanical profilers. Appl Opt 36:9005–9009
11. Lee C-O, Park K, Park BC, Lee YW (2005) An algorithm for stylus instruments to measure aspheric surfaces. Meas Sci Technol 16:1215
12. Lee DH (2013) 3-dimensional profile distortion measured by stylus type. Measurement 46:803–814
13. Fang H, Xu B, Chen W, Tang H, Zhao S (2015) A slope-adapted sample-tilting method for profile measurement of microstructures with steep surfaces. J Nanomater ID 253062 (in press)
14. Hocken RJ, Pereira PH (eds) (2011) Coordinate measuring machines and systems, 2nd edn. CRC Press, New York
15. ISO 10360 part 3 (2000) Geometrical product specifications (GPS)—acceptance and reverification tests for coordinate measuring machines (CMM)—Part 3: CMMs with the axis of a rotary table as the fourth axis. International Organization for Standardization
16. Vermeulen MMPA, Rosielle PCJN, Schellekens PHJ (1998) Design of a high-precision 3D-coordinate measuring machine. Ann CIRP 47:447–450
17. Widdershoven I, Donker RL, Spaan HAM (2011) Realization and calibration of the "Isara 400" ultra-precision CMM. J Phys: Conf Ser 311:012002
18. Jäger G, Manske E, Hausotte T, Büchner H-J, Grünwald R, Schott W (2001) Nanomeasuring technology—nanomeasuring machine. In: Proceedings of the ASPE, Crystal City, VA, Nov. 2001, pp 23–27
19. Leach RK (2015) Abbe error/offset. In: Laperrière L, Reinhart G (eds) CIRP encyclopaedia of production engineering. Springer, Berlin
20. Fan K-C, Fei Y-T, Wang W, Chen Y, Chen Y-C (2008) Micro-CMM. In: Smart devices and machines for advanced manufacturing, pp 319–335
21. Claverley JD, Leach RK (2015) A review of the existing performance verification infrastructure for micro-CMMs. Precis Eng 39:1–15
22. ISO 10360 part 1 (2001) Geometrical product specifications (GPS)—acceptance and reverification tests for coordinate measuring machines (CMM). International Organization for Standardization
23. Weckenmann A, Estler T, Peggs G, McMurtry D (2004) Probing systems in dimensional metrology. Ann CIRP 53:657–684
24. Küng A, Meli F, Thalmann R (2007) Ultraprecision micro-CMM using a low force 3D touch probe. Measur Sci Technol 18:319–327
25. Chu C-L, Chiu C-Y (2007) Development of a low-cost nanoscale touch trigger probe based on two commercial DVD pick-up heads. Measur Sci Technol 18:1831–1842
26. Haitjema H, Pril WO, Schellekens PHJ (2001) Development of a silicon-based nanoprobe system for 3-D measurements. Ann CIRP 50:365–368
27. Brand U, Kleine-Besten T, Schwenke H (2000) Development of a special CMM for dimensional metrology on microsystem components. In: Proceedings of the ASPE, Scottsdale, AZ, Oct. 2000, pp 542–546
28. Ruther P, Bartholomeyczik J, Trautmann A, Wandt M, Pau O, Dominicus W, Roth R, Seitz K, Strauss W (2005) Novel 3D piezoresistive silicon force sensor for dimensional metrology of micro components. In: Proceedings of the IEEE sensor, pp 1006–1009

29. Dai G, Bütefisch S, Pohlenz F, Danzebrink H-U (2009) A high precision micro/nano CMM using piezoresistive tactile probes. Measur Sci Technol 20:084001
30. Muralikrishnan B, Stone J, Stoup J (2007) Roundness measurements using the NIST fibre probe. In: Proceedings of the ASPE, Dallas, TX, Oct. 2007, pp 89–92
31. Takaya Y, Takahashi S, Miyoshi T, Saito K (1999) Development of the nano-CMM probe based on laser trapping technology. Ann CIRP 48:421–424
32. Seugling R, Darnell I (2008) Investigating scaling limits of a fibre based resonant probe for metrology applications. In: Proceedings of the ASPE, Livermore, CA, Oct. 2008
33. Claverley JD, Leach RK (2013) Development of a three-dimensional vibrating tactile probe for miniature CMMs. Precis Eng 37:491–499
34. Lee ES, Burdekin M (2001) A hole plate artifact design for volumetric error calibration of a CMM. Int J Adv Manuf Technol 17:508–515
35. Schwenke H, Franke M, Hannaford J, Kunzmann H (2005) Error mapping of CMMs and machine tools by a single tracking interferometer. Ann CIRP 54:475–478
36. Schwenke H, Knapp W, Haitjema H, Weckenmann A, Schmitt R, Delbressine F (2008) Geometric error measurement and compensation for machines—an update. Ann CIRP 57:660–675
37. Zhang G, Veale R, Charlton T, Borchardt B, Hocken R (1985) Error compensation of coordinate measuring machines. Ann CIRP 34:445–448
38. Krutha J-P, Vanhercka P, Van den Bergha C (2001) Compensation of static and transient thermal errors on CMMs. Ann CIRP 50:377–380
39. Aggogeri F, Barbato G, Barini EM, Genta G, Levi R (2011) Measurement uncertainty assessment of coordinate measuring machines by simulation and planned experimentation. CIRP-JMST 4:51–56
40. ISO 10360 part 6 (2001) Geometrical product specifications (GPS)—acceptance and reverification tests for coordinate measuring machines (CMM)—Part 6: estimation of errors in computing Gaussian associated features. International Organization for Standardization
41. Danzl R, Helmli F, Rubert P, Prantl M (2008) Optical roughness measurements on specially designed roughness standards. Proc SPIE 7102:71020M
42. Hemli F (2011) Focus-variation instruments. In: Leach RK (ed) Optical measurement of surface topography. Springer, Berlin
43. Scherer S (2007) Focus-variation for optical 3D measurement in the micro- and nano-range. In: Bauer N (ed) Handbuch zur Industriellen Bildverarbeitung. Fraunhofer IRB Verlag, Stuttgart
44. Zhang Y, Zhang Y, Wen CY (2000) A new focus measure method using moments. Image Vision Comput 18:959–965
45. Helmli FS, Scherer S (2001) Adaptive shape from focus with an error estimation in light microscopy. In: ISPA 2001, Pula, Croatia, June 2001, pp 188–193
46. Danzl R, Helmli F, Scherer S (2011) Focus variation—a robust technology for high resolution optical 3D surface metrology. J Mech Eng 57:245–256
47. ISO 25178 part 604 (2001) Geometrical product specification (GPS)—surface texture: Areal–Part 604: Nominal characteristics of non-contact (coherence scanning interferometry) instruments. International Organization for Standardization
48. de Groot P (2011) Coherence scanning interferometry. In: Leach RK (ed) Optical measurement of surface topography, vol 9. Springer, Berlin
49. de Groot P (2015) Principles of interference microscopy for the measurement of surface topography. Adv Opt Photon 7:1–65
50. de Groot P, Colonna de Lega X, Kramer J, Turzhitsky M (2002) Determination of fringe order in white-light interference microscopy. Appl Opt 41:4571–4578
51. Colonna de Lega X, Biegen J, de Groot P, Häusler G, Andretzky P (2003) Large field-of-view scanning white-light interferometers. In: Proceedings of the ASPE, Portland, OR, Oct. 2003, p 1275
52. Wyant JC, Schmit J (1998) Large field of view, high spatial resolution, surface measurements. Int J Mach Tools Manuf 38:691–698

53. Gao F, Leach RK, Petzing J, Coupland JM (2008) Surface measurement errors using commercial scanning white light interferometers. Measur Sci Technol 19:015303
54. Schwider J, Zhou L (1994) Dispersive interferometric profilometer. Opt Lett 19:995–997
55. Marron JC, Gleichman KW (2000) Three-dimensional imaging using a tunable laser source. Opt Eng 39:47–51
56. Jiang X (2012) Precision surface measurement. Phil Trans R Soc A 370:4089–4114
57. Paz VF, Peterhänsel S, Frenner K, Osten W (2012) Solving the inverse grating problem by white light interference Fourier scatterometry. Light: Sci Appl 1:e36
58. Colonna de Lega X, de Groot P (2005) Optical topography measurement of patterned wafers. AIP Conf Proc 788:432–436
59. Minsky M (1961) Microscopy apparatus. US patent, vol US3013467A
60. Minsky M (1988) Memoir on inventing the confocal microscope. Scanning 10:128–138
61. Wilson T (ed) (1990) Confocal microscopy. Academic Press, London
62. Diaspro A (ed) (2002) Confocal and two—photon microscopy: foundations, applications, and advances. Wiley-Liss, New York
63. Hibbs AR (2004) Confocal microscopy for biologists. Kluwer Press, New York
64. Artigas R (2001) Imaging confocal microscopy. In: Leach RK (ed) Optical measurement of surface topography. Springer, Berlin
65. Semwogere D, Weeks ER (2005) Confocal microscopy. In: Encyclopedia of biomaterials and biomedical engineering. Taylor&Francis, London
66. Brakenhoff GJ, Blom P, Barends P (1976) Confocal scanning light microscopy with high aperture immersion lenses. J Microsc 117:21932
67. Wilson T (2011) Resolution and optical sectioning in the confocal microscope. J Microsc 244:113–121
68. Leach RK (ed) (2011) Optical measurement of surface topography. Springer, Berlin, Germany
69. Muralikrishnan B, Ren W, Everett D, Stanfield E, Doiron T (2011) Dimensional metrology of bipolar fuel cell plates using laser spot triangulation probes. Meas Sci Technol 22:075102
70. Kjaer KH, Ottose C-O (2015) 3D laser triangulation for plant phenotyping in challenging environments. Sensors 15:13533–13547
71. Peiravi A, Taabbodi B (2010) A reliable 3D laser triangulation-based scanner with a new simple but accurate procedure for finding scanner parameters. J Am Sci 6:80
72. Clarke TA, Grattan KTV, Lindsey NE (1991) Laser-based triangulation techniques in optical inspection of industrial structures. Proc SPIE 1332:474–486
73. MacKinnon D, Beraldin J-A, Cournoyer L, Picard M, Blais F (2012) Lateral resolution challenges for triangulation-based three-dimensional imaging systems. Opt Eng 51:021111
74. Zeng L, Matsumoto H, Kawachi K (1997) Two-directional scanning method for reducing the shadow effects in laser triangulation. Measur Sci Technol 8:262–266
75. Gorthi SS, Rastogi P (2010) Fringe projection techniques: whither we are? Opt Lasers Eng 48(2):133–140
76. Leonhardt K, Droste U, Tiziani HJ (1994) Micro shape and rough-surface analysis by fringe projection. Appl Opt 33:7477–7488
77. Quan C, Tay CJ, He XY, Kang X, Shang HM (2002) Microscopic surface contouring by fringe projection method. Opt Laser Technol 34(7):547–552
78. Chen L-C, Liao C-C, Lai M-J (2005) Full-field micro surface profilometry using digital fringe projection with spatial encoding principle. J Phys: Conf Series 13:147–150
79. He X, Sun W, Zheng X, Nie M (2006) Static and dynamic deformation measurements of micro beams by the technique of digital image correlation. Key Eng Mater 326–328:211–214
80. Chen L, Chang Y (2008) High accuracy confocal full-field 3-D surface profilometry for micro lenses using a digital fringe projection strategy. Key Eng Mater 364–366:113–116
81. Li A, Peng X, Yina Y, Liua X, Zhao Q, Körner K, Osten W (2013) Fringe projection based quantitative 3D microscopy. Optik 124:5052–5056

82. Yin Y, Wang M, Gao BZ, Liu X, Peng X (2015) Fringe projection 3D microscopy with the general imaging model. Opt Express 23:6846
83. Chen J, Guo T, Wang L, Wu Z, Fu X, Hu X (2013) Microscopic fringe projection system and measuring method. Proc SPIE 8759:87594U
84. Drexler W, Fujimoto JG (eds) (2008) Optical coherence tomography: technology and applications. Springer, Berlin
85. Stifter D (2007) Beyond biomedicine: a review of alternative applications and developments for optical coherence tomography. Appl Phys B 88:337–357
86. Guan G, Hirsch M, Lu ZH, Childs DT, Matcher SJ, Goodridge R, Groom KM, Clare AT (2015) Evaluation of selective laser sintering processes by optical coherence tomography. J: Mater Design (accepted)
87. Wieser W, Biedermann BR, Klein T, Eigenwillig CM, Huber R (2010) Multi-megahertz OCT: high quality 3D imaging at 20 million A-scans and 4.5 GVoxels per second. Opt Express 18:14685–14704
88. Czajkowski J, Vilmi P, Lauri J, Sliz R, Fabritius T, Myllylä R (2012) Characterization of ink-jet printed RGB color filters with spectral domain optical coherence tomography. Proc SPIE 8496:849308
89. Thrane L, Jørgensen TM, Jørgensen M, Krebs FC (2012) Application of optical coherence tomography (OCT) as a 3-dimensional imaging technique for roll-to-roll coated polymer solar cells. Solar Energy Mater Solar Cells 97:181–185
90. Su R, Kirillin M, Ekberg P, Mattsson L (2015) Three-dimensional metrology of embedded microfeatures in ceramics by infra-red optical coherence tomography—advantages and limitations. In: Proceedings of the 11th LAMDAMAP, March 2015. Swindon, UK, pp 74–83
91. Ahn Y, Jung W, Chen Z (2008) Optical sectioning for microfluidics: secondary flow and mixing in a meandering microchannel. Lab Chip 8:125–133
92. Stifter D, Leiss-Holzinger E, Major Z, Baumann B, Pircher M, Götzinger E, Hitzenberger CK, Heise B (2010) Dynamic optical studies in materials testing with spectral-domain polarization-sensitive optical coherence tomography. Opt Express 18:25712–25725
93. Dubois A, Grieve K, Moneron G, Lecaque R, Vabre L, Boccara C (2004) Ultrahigh-resolution full-field optical coherence tomography. Appl Opt 43:2874–2883
94. Chen T, Zhang N, Huo T, Wang C, Zheng J, Zhou T, Xue P (2013) Tiny endoscopic optical coherence tomography probe driven by a miniaturized hollow ultrasonic motor. J Biomed Opt 18:086011
95. Prylepa A, Duchoslav J, Keppert T, Luckeneder G, Stellnberger K-H, Stifter D (2013) Nonlinear imaging with interferometric SHG microscopy using a broadband 1550 nm fs-fiber laser. In: CLEO EUROPE/IQEC, Munich, Germany, May 2013, p 1
96. Su R, Kirillin M, Chang EW, Sergeeva E, Yun SH, Mattsson L (2014) Perspectives of mid-infrared optical coherence tomography for inspection and micrometrology of industrial ceramics. Opt Express 22:15804–15819
97. Schmitt JM, Xiang SH, Yung KM (1999) Speckle in optical coherence tomography. J Biomed Opt 4:95–105
98. Hitzenberger CK, Baumgartner A, Fercher AF (1998) Dispersion in-duced multiple signal peak splitting in partial coherence interferometry. Opt Commun 154:179–185
99. Su R, Ekberg P, Leitner M, Mattsson L (2014) Accurate and automated image segmentation of 3D optical coherence tomography data suffering from low signal-to-noise levels. J Opt Soc Am A 31:2551–2560
100. Chiffre LD, Carmignato S, Kruth J-P, Schmit R, Wecken-mann A (2014) Industrial applications of computed tomography. Ann CIRP 63:655–677
101. Kruth JP, Bartscher M, Carmignato S, Schmitt R, Chiffre LD, Weckenmannf A (2011) Computed tomography for dimensional metrology. Ann CIRP 60:821–842
102. Hsieh J (2009) Computed tomography: principles, design, artifacts, and recent advances, 2nd edn. SPIE Press, Bellingham

103. Boone JM (2000) X-ray production, interaction, and detection in diagnostic imaging. In: Beutel J, Kundel HL, Van Metter RL (eds) Handbook of medical imaging, physics and psychophysics. SPIE Press, Bellingham, pp 1–78
104. Requena G, Cloetens P, Altendorfer W, Poletti C, Tolnai D, Warchomickaa F, Degischera HP (2009) Sub-micrometer synchrotron tomography of multiphase metals using Kirkpatrick-Baez optics. Scripta Mater 61:760–763
105. Yaffe MJ, Rowlands JA (1997) X-ray detectors for digital radiography. Phys Med Biol 42:1–39
106. Smith BD (1990) Cone-beam tomography: recent advances and a tutorial review. Opt Eng 29:524–534
107. Ferrucci M, Leach RK, Giusca C, Carmignato S, Dewulf W (2015) Towards geometrical calibration of x-ray computed tomography systems—a review. Meas Sci Technol 26:092003
108. Flay N, Sun W, Brown S, Leach RK, Blumensat T (2015) Investigation of the focal spot drift in industrial cone-beam x-ray computed tomography. In: Proceedings of the DIR 2015, Ghent, Belgium, June 2015
109. Brooks RA, Di Chiro G (1976) Beam hardening in x-ray reconstructive tomography. Phys Med Biol 21:390–398
110. Santiago P, Gage HD (1995) Statistical-models of partial volume effect. IEEE Trans Image Processing 4:1531–1540
111. Schorner K, Goldammer M, Stephan J (2011) Comparison between beam-stop and beam-hole array scatter correction techniques for industrial X-ray cone-beam CT. Nucl Instrum Meth B 269:292–299
112. Mail N, Moseley DJ, Siewerdsen JH, Jaffray DA (2008) An empirical method for lag correction in cone-beam CT. Med Phys 35:5187–5196
113. Carmignato S, Pierobon A, Savio E (2011) First international intercomparison of computed tomography systems for dimensional metrology. In: Proceedings of the 11th Euspen international conference, Como, Italy, May 2011. pp 84–87
114. Dewulf W, Kiekens K, Tan Y, Welkenhuyzen F, Kruth J-P (2013) Uncertainty determination and quantification for dimensional measurements with industrial computed tomography. Ann CIRP 62:535–538
115. Hiller J, Maisl M, Reindl LM (2012) Physical characterization and performance evaluation of an X-ray micro-computed tomography system for dimensional metrology applications. Measur Sci Technol 23:085404
116. Hsieh J, Chao E, Thibault J, Grekowicz B, Horst A, McOlash S, Myers TJ (2004) A novel reconstruction algorithm to extend the CT scan field-of-view. Med Phys 31:2385–2391
117. Krämer P, Weckenmann A (2010) Multi-energy image stack fusion in computed tomography. Measur Sci Technol 21:045105
118. Fitzgerald R (2007) Phase-sensitive x-ray imaging. Phys Today 53:23–26
119. Flay N, Leach RK (2012) Application of the optical transfer function in x-ray computed tomography—a review. NPL Report ENG 41
120. Landis EN, Keane DT (2010) X-ray microtomography. Mater Charact 61:1305–1316